5

Impact of Defect Structure on 'Bulk' and Nano-Scale Ferroelectrics

Emre Erdem and Rüdiger-A. Eichel
Institut für Physikalische Chemie I, Universität Freiburg, Albertstr. 21, D-79104 Freiburg Germany

1. Introduction

Ferroelectric materials offer a wide range of dedicated physical properties such as high dielectric constant, spontaneous polarisation, pyroelectric and piezoelectric effects which can be applied in thin-film non-volatile memories or 'bulk' actuators, multi-layer capacitors, thermal sensors and transducers (1–3). In that respect, desired materials properties for specific applications may be tailored by controlling the defect structure by means of aliovalent doping, rendering so-termed '*hard*' or '*soft*' piezoelectric materials (4–6).
Another important impact on ferroelectric properties results from the confined size in nano-scale architectures (7). At the nanometer scale physical and chemical properties are expected to differ markedly from those of the 'bulk' material. Owing to a *size-driven phase transition*, a critical particle size exists below which ferroelectricity does no longer occur (8).
In this chapter, we will first outline the nature of the *size-driven* para-to-ferroelectric phase transition, as well as the concepts of *defect chemistry*. On that basis, the interplay between confined size at the nano-regime and the development of defect structure will be characterized. The here studied ferroelectric lead titanate nano-powders may be considered as a model system for more complex ferroelectric nano architectures (1; 2). Furthermore, the results discussed here may be transferred to large extent to other important perovskite oxides with divalent A- and tetravalent B-site, such as $BaTiO_3$ or $Pb[Zr,Ti]O_3$ (PZT). The defect chemistry of ferroelectric perovskite oxides with monovalent A- and pentavalent B-site, such as the $[K,Na]NbO_3$ (KNN) solid solution system, however has shown some important deviations from the defect structure characterized for PZT compounds (9; 10).

2. Synthesis of perovskite oxide nano-powders

Many different strategies have been employed in recent years to synthesize ferroelectric nano-powders. These include hydrothermal (11), alkoxide (12), co-precipitation (13) and sol-gel (14) techniques. The main drawback associated with the above-mentioned routes is the agglomeration of particles, which prevents the synthesis of ultra-fine nano-powders. This problem may be overcome by two alternative methods – the *combined polymerization and pyrolysis* (CPP) technique (15; 16) and the *high-energy ball milling* (HEBM) cold mechanical alloying (17; 18). In particular, both methods provide the opportunity to homogeneously incorporate aliovalent transition-metal or rare-earth dopants with concentrations ranging between $10^{-2} - 10^{0}$ mol%.

2.1 Combined polymerization and pyrolysis

The CPP-route starts from a monomeric metallo-organic precursor through combined solid-state polymerisation and pyrolysis (15; 16). Adjustment of various mean particle sizes is obtained by choosing appropriate calcination temperatures. A remarkable optimization of the CPP route is obtained by applying special tempering conditions, e.g. oxidative atmosphere or quenching into a non-equilibrium state. With this technique, ultrafine $PbTiO_3$ powders down to 5 nm mean grain size result (15). CPP based nano-particles are characterized by a comparatively high reaction homogeneity, particularly in the polymerization step. The particle sizes may further by decreased by subsequently applying to high energy ball milling. Recent results of the CPP technique include the synthesis of nano-scale $BaTiO_3$ (19) and $PbTiO_3$ powders (15; 16) with mean particle sizes ranging from 150 nm down to 5 nm.

The corresponding results from differential thermogravimetric analysis (DTA) (weight loss, blue line) and differential scanning calorimetry (DSC) (thermal change) of the CPP precursor are given in figure 1(a). The TGA results show exothermic changes in specific temperatures (assigned in figure 1(a)) of the precursor due to the CPP formation reactions, as well as evaporation of various volatiles and phase changes of the crystal. The CPP of $PbTiO_3$ is initialized around 510 K and peaking at 530 K coupled by the polymerization of $-C = C-$ double bonds in the methyacrylate part of the ligand from the precursor (15). The pyrolysis of the hydrocarbons occurs at 554 K and is followed by formation of $PbTiO_3$ (T_{max} = 554 K) while release of carbon and other volatiles processed. The deconvolution of the two main overlapping peaks between $740 - 770$ K corresponds to the complete combustion and evaporation of amorphous organic residues (753 K). The ferro-to-paraelectric phase transition occurs at the Curie temperature for $PbTiO_3$ (763 K). Further heating of the sample gives rise to mass losses due to PbO evaporization.

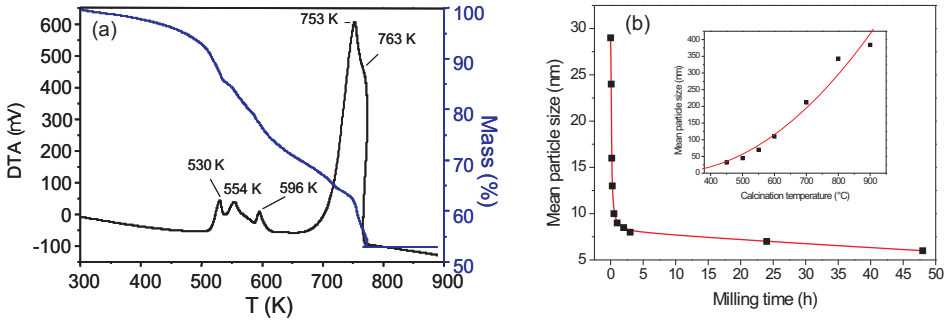

Fig. 1. (a) - differential thermogravimetric analysis (weight loss) and differential scanning calorimetry (thermal change) of the precursor. (b) - mean particle size as function of calcination temperature. The inset shows the variation in mean particle size as function of different ball-milling times.

As function of calcination temperature, the mean particle size of the nano-powders can be controlled, as shown in figure 1(b). The corresponding mechanism is the following: (*i*) a low calcination temperatures gives the smallest particle size and increasing the temperature gives much larger patrticle size, (*ii*) applying additionally high-energy ball milling to the smallest particles obtained after calcination, even smaller particle sizes result (see inset in figure 1(b)). Moreover, this method allows to introduce dopants by resolving the corresponding metal

ions into the solution. In addition it is observed that after calcination the solid-state solution exhibits a rate of homogeneous.
A special advantageous feature of the CPP-preparation route is its ability to introduce small amounts of dopant ions, such as Cr^{3+}, Mn^{2+}, Fe^{3+}, Cu^{2+} or Gd^{3+} for instance, by just adding the corresponding metal acetates to the monomeric precursor.
Although the CPP-route offers a flexible preparation technique to obtain different mean particle sizes as function of appropriate calcination temperature and atmosphere, the particle-size distribution typically is rather broad. In addition to that, nano-particles below 20 nm proved being largely amorphous. These problems can be circumvented by performing ball milling subsequent to the CPP-route. The most important advantages of CPP-route are its excellent control over particle size, shape and morphology (phase purity) by adjusting the calcination temperature.

2.2 High-energy ball milling

An alternative strategy to synthesize nano-grained ferroelectric compounds is the use of cold mechanical alloying by means of high-energy ball milling. Varying mean grain sized can be obtained by different milling times. The here presented HEBM nano-powders were obtained for milling times in an interval between milling times 1 and 50 h at a speed of 300 rpm and a ball-to-powder weight ratio of 10:1.
The advantage over the above mentioned CPP-route, which requires a calcination step at an elevated temperature to convert the precursor into the ferroelectric phase, is that this technique virtually is performed at ambient temperature. Furthermore, there is no need of high-purity inorganic or organometallic chemicals for the starting materials, thus offering an inexpensive processing route and additionally overcoming problems associated with high sensitivity to moisture which typically requires special precaution and handling.
An advantage in common concerning the use of ferroelectric nano-powders as compared to the standard high-temperature mixed-oxide solid-state reaction techniques is that dense ceramics may be obtained at considerably lower sintering temperatures owing to the inherent high rate of homogeneity of the synthesized nano-powders. This argument particularly is relevant for the synthesis of lead-containing ferroelectric compounds, such that the loss of PbO at high temperatures can be markedly reduced.

3. Size-driven para-to-ferroelectric phase transition

The most prominent impact of lead titanate nano-powders is that a *size-driven phase transition* from the ferroelectric to the paraelectric state can be observed below a critical mean particle size at ambient temperature. In the following section, we briefly outline the theoretical foundations describing the size-driven phase transition by means of the Landau-Ginzburg theory, as well as summarize experimental results monitoring the phase transition on various length scales.

3.1 Landau-Ginzburg theoretical description of the size-driven phase transition

The phenomenological *Landau-Ginzburg theory* (LGT) furnishes a systematic basis to discuss the phase transition properties of bulk ferroelectrics (20–22). In recent years several attempts were made to extend the LGT to nanolayers (23–25) and nanoparticles (26–31). Starting from the total free energy of a infinite-size and homogeneous ferroelectric, the latter two gradient and surface terms were added for a finite-size ferroelectric particle

$$F = \int_V dV \left[\frac{1}{2}A'(T - T_C)P^2 + \frac{1}{4}B'P^4 + \frac{1}{6}C'P^6 + \frac{1}{2}D'(\nabla P)^2\right] + \frac{D'}{2\delta}\int_S dS\ P^2 \qquad (1)$$

Obviously, the gradient and surface terms are only of relevance in an outer shell. They comprise the surface field contribution in the formation of the polarisation gradient. The effect of the surface on the polarisation is taken into account through the concept of the extrapolation length d (24; 26; 27). In solving the pertinent *Euler-Lagrange* equation for minimising the free energy, the polarisation is obtained considering the boundary condition according to the extrapolation length conception.

The size dependence of the polarization and the Curie temperature of ferroelectric particles with a first-order transition were studied in the previous study (8) where different polarization quantities refer to (i) polarisation at the particle centre (ii) average polarization of the particle (iii) polarization at the particles outer boundary, and (iv) polarisation difference between particle centre and border.

Because of the electrostrictive coupling between lattice strain and polarization in perovskite-type ABO_3 systems, the deformation of the tetragonal unit cell depends on the polarization, and particularly the tetragonality $(\frac{c}{a} - 1)$ is proportional to the square of P_s (32). As a result, the variation of P_s involves a change of the c/a-ratio near the nano-particle surface. For $PbTiO_3$ nano-particles, the LGT predicts a critical size of $d_{\text{crit}}^{\text{LGT}} = 4.2$ nm (26), whereas the hitherto experimentally estimated critical size amounts to $d_{\text{crit}}^{\text{exp}} = 12.6$ nm (33). This discrepancy for controversial values of d_{crit} can be attributed to the polarization gradient, a nano-crystalline surface layer and the depolarization effect. The effect of a depolarization field (E_d) and a space-charge layer on the Curie temperature T_C shift was comprised within a finite-size multi-domain model of a cubic ferroelectric particle (34). On the other hand, a phenomenological theory of the size-dependent dielectric susceptibility (28) was based on spherical ferroelectric particles, thereby unfortunately disregarding the surface energy which plays a decisive role in the physics of nano-materials. Finally a model was proposed (30) which gives due consideration to the depolarisation field E_d and also includes the surface and domain-wall energies.

However, a homogeneous comprehensive theory was not yet elaborated so far, and existing models yield rather scattering d_{crit} values. Nevertheless, very recent Landau phenomenological theory calculations for confined ferroelectric nanoparticles are very good agreement with experimental results (35).

3.2 X-ray diffraction

The size-driven phase transition can be directly monitored by considering the corresponding XRD patterns of the nano-powders as function of mean grain size. In figure 2 the XRD patterns of nano-powders obtained by CPP and HEBM are compared to each other.

All observed reflexes can be explained by the perovskite structure. For the 'bulk' $PbTiO_3$ component, the corresponding reflexes are indexed. In figure 2(a) the XRD patterns for the nano-powders obtained from CPP are shown. All nano-powders exhibit Bragg reflexes characteristic for the $PbTiO_3$ crystal structure. With decreasing mean particle size, the (001) and (100) reflexes that belong to the crystalline lattice constants, a and c, approach each other. This indicates the corresponding size-driven ferro-to-paraelectric phase transition from tetragonal to cubic crystal symmetry. Furthermore, for the nano-scale particles, the reflexes are considerably broadened, which hinders further structural refinement.

Figure 2(b) compares the XRD patterns for nano-powders obtained by HEBM for varying milling times. The determined c/a-ratio of the $PbTiO_3$ powders decreases from 85 to 20 nm, when varying the milling time from 30 to 50 h.

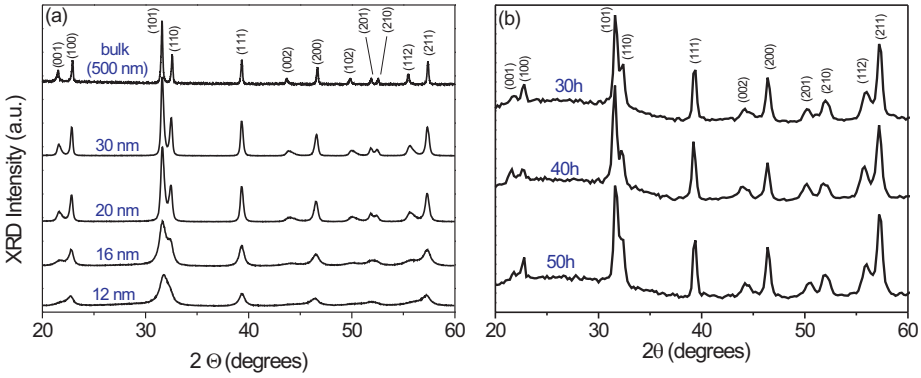

Fig. 2. XRD patterns lead titanate nano-powders as function of mean grain size. (a) - $PbTiO_3$ nano-powders as synthesized by the CPP-route for varying calcination temperatures. (b) - $PbTiO_3$ nano-powders as synthesized by HEBM for varying milling times.

3.3 Raman spectroscopy

A microscopic description of the ferroelectric behavior requires the consideration of lattice dynamics by means of the *soft-mode theory*. Accordingly, in the ferroelectric phase the $PbTiO_3$ cations are displaced from the centre of the anion lattice, resulting in an inner electric field with a permanent electric moment and a spontaneous polarization. Contrary, in the paraelectric phase $PbTiO_3$ has cubic symmetry and can be polarized along any of the three equivalent 4^{th}-order axes. Upon the transition to the tetragonal symmetry, one direction is chosen as the crystallographic *c*-axis and is associated with a characteristic lattice vibrational mode, either acoustic or optical. In the paraelectric phase all ions move collectively with the same phase, whereas in the ferroelectric phase anions and cations move independently of each other with opposite phases. Both modes can be of longitudinal or transversal type and their frequency depends on temperature. When a ferroelectric phase transition takes place, the transversal optical mode exhibits an instability and its frequency decreases towards zero, i.e. it 'softens'. At T_C the mode is 'frozen' and the mode frequency reaches zero. This enables a rise of a non-zero order parameter and lowers the crystal symmetry. Such a vibrational mode is called '*soft mode*'. In case of nano-particles it is aimed that softening occurs not by temperature but by reduction of lattice parameters, hence particle size.

Correspondingly, Raman spectroscopy can be employed to study the occurrence of soft mode as function of mean grain-size. The corresponding Raman-spectra are depicted in figure 3. In figure 3(a) the Raman spectra as function of mean particle size are shown, where the corresponding phonon modes are assigned according to 'bulk' $PbTiO_3$ (36).

Assuming a strong correlation between the crystalline unit-cell dimensions (*a*, *c*) and the longitudinal optical (LO) and transversal optical (TO) phonon modes, with decreasing mean particle size, the LO modes shift to higher wave numbers whereas the TO modes are shifted to lower wave numbers. More importantly, the soft-mode becomes weaker for small particle sizes and finally disappears below a critical particle diameter, d_{crit}, indicating the transition from a ferroelectric to a paraelectric nano-powder. This observation may be explained by considering that for nano-sized compounds the quotient between number of atoms at the

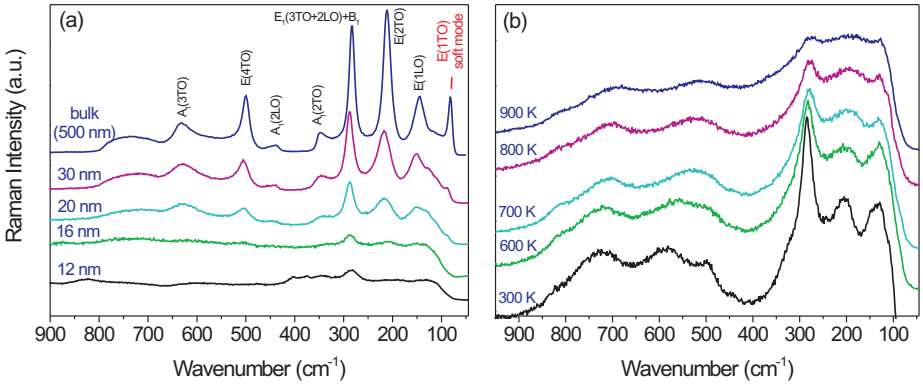

Fig. 3. Raman spectra of $PbTiO_3$. (a) - Raman spectra as function of mean grain size. (b) - Raman spectra as function of temperature.

surface and atoms in the bulk markedly increases. Accordingly, short-range forces become more dominant as compared to long range forces. As a consequence, a *size-driven phase transition* occurs, such that the Curie temperature for bulk $PbTiO_3$, $T_C = 766$ K is reduced to a value below ambient temperature.
This size-driven phase transition is compared to a temperature-induced phase transition for a specimen of 16 nm mean grain size (cf. (figure 3(b)). By increasing the measuring temperature similar Raman lines occur as observed fo a 'bulk' sample. However, above 700 K the Raman lines start to disappear. This is around 60 K lower than the value of bulk T_C, indicating a reduction in the value of T_C at 16 nm mean grain size.

3.4 X-ray Absorption Near Edge Structure

The size dependent X-ray Absorption Near Edge Structure (XANES) of $PbTiO_3$ gives significant information about the nature of phase transitions. We find that we can quantitatively relate the local structure of several Ti perovskites with the pre-edge and post-edge peaks in their XANES spectra. Here, the size effect on Ti *K*- edge and Pb *L*3-edge XANES spectra is investigated. In order to characterize the local structure of the $PbTiO_3$ nano-powders, XANES at Ti *K*-edge and Pb *L*3-edge was compared to the 'bulk' compounds. The corresponding XANES-spectra are shown in figure 4. The pre-edge features (labeled as **A** and **B** in figure 4) are atrributed to quadrupolar transitions of t_{2g}-type orbitals situated in the absorption Ti-atom (37). The transition **A** is caused by hybridization of $p-$ and d-symmetry states at the Ti-atom under the influence of the neighboring oxygen atoms that takes place if the inversion symmetry is broken relative to the absorbing atom position (37). The pre-edge feature **B** is refered to the Ti 1s-electron transition to the unoccupied 3d-states of the neighbouring Ti-atoms and the transition occurs if there are 4d-atoms in the neighbourhood of the absorbing Ti-atom (37; 38).
The transitions labeled **C**, **D**, **E**, **F** and **G** at energies above the absorption edge are related to electronic transitions and to the atomic structure of second and third-nearest neighbours of Ti within distances up to 1.0 nm (37; 38). The pre-edge features labeled as **C**, **E** and **F** in the spectrum for the bulk ferroelectric do not appear in the spectrum for the nano-structured sample.

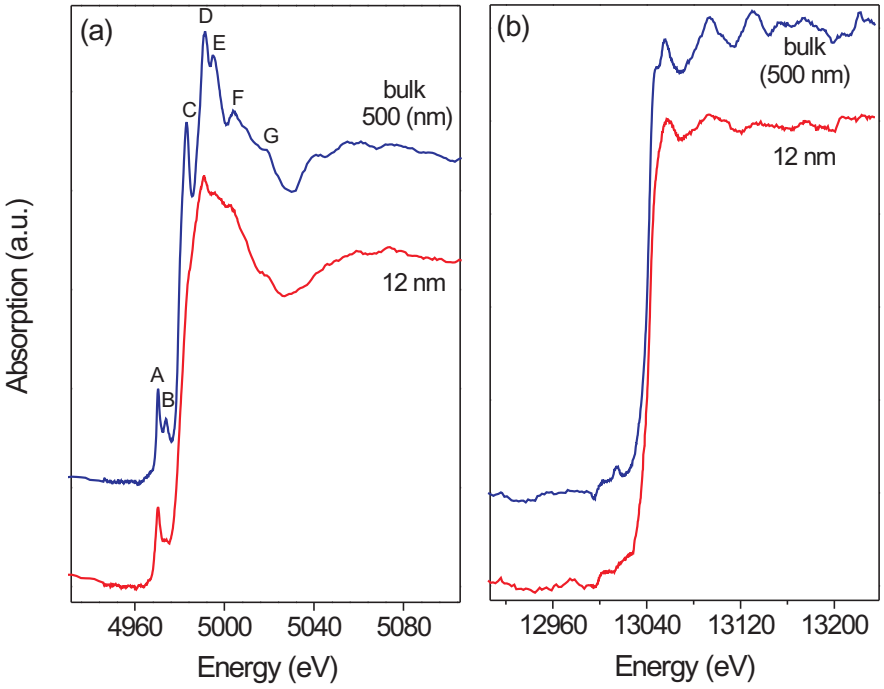

Fig. 4. X-ray Absorption Near Edge Structure spectra of 'bulk' and nano-scale $PbTiO_3$ powders. (a) - Ti *K*-edge. (b) - Pb L_3-edge.

It is noteworthy to say that the experimental results that we obtained are in very good agreement with the simulation of XANES spectra given in literature (37). Pb *L*3-edge XANES spectrum showed in Figure 4 the absorption features after the edge are related to the internal transitions between the 2p and the empty d states in Pb^{2+} ions (37).
Overall, as compared with the 'bulk' sample (500 nm), the 12 nm sample yields broadened spectral features, concerning pre-edge structures (**A**-**D**) and the post-edge (**E**-**G**) structures. Clearly, if the mean particle size falls below a critical value (ca. 6 nm), any translational symmetry is largely removed and the idea of persistent tetragonal structural units no longer stays. Changing of symmetry translates into more diffuse scattering pathways and results in the smearing of Ti *K*- edge XANES features, indicating structural transition from tetragonal phase to cubic phase, in other words a transition from ferroelectric-to-paraelectric phase.

3.5 EPR-spectroscopy

In order to monitor the size-driven phase transition on an atomic level, electron paramagnetic resonance (EPR) spectroscopy has been applied. As a paramagnetic probe ion Cr^{3+} has been incorporated into the $PbTiO_3$ lattice (15). In that respect, Cr^{3+} is a very suitable probe ion, because ionic size is very close to that of Ti^{4+} and furthermore, trivalent Cr^{3+} is a high-spin

ion ($S = \frac{3}{2}$) which sensitively probes subtle structural changes by means of its quadrupole fine-structure interaction.
The corresponding EPR spectra for Cr^{3+}-doped $PbTiO_3$ nano-powders are illustrated in figure 5(a) for varying mean particle sizes, as compared to a bulk Cr^{3+}:$PbTiO_3$ compound measured at varying temperature (cf. figure 5(b)).
First, the *size-driven phase transition* of Cr^{3+}:$PbTiO_3$ nano-powders is considered (figure 5(b,d)). For nano-powders of mean grain-size above a critical value ($d > d_{crit}$), the EPR spectra are characteristic of a central transition and satellite transitions. This situation points to an axial site symmetry at the Cr^{3+}-site, indicating tetragonal symmetry of the Cr^{3+}:$PbTiO_3$ nano-powders. Upon reduced mean grain size, the splitting of the satellite resonances monotonically reduces, until a single resonance emerges at $d \leq d_{crit}$. This situation only occurs if the fine-structure interaction vanishes, which is valid only for cubic symmetry. The corresponding size-driven phase transition is illustrated by exploiting the variation of the axial fine-structure parameters D as function of mean grain size (cf. figure 5(d)).
As comparison, in figure 5(a,c), the *temperature-induced phase transition* of bulk Cr^{3+}:$PbTiO_3$ is shown. A similar behavior for the splitting of satellite resonances for temperatures below T_C is observed, where the single-line situation characteristic for the paraelectric state is observed for temperatures above the Curie temperature, $T \geq T_C = 765$ K.
Both phase transitions show a first-order character (8; 15).

3.6 Core-Shell structural model for nano-scale ferroelectrics

As a structure model of the spherical nanoparticles to give a comprehensive explanation for the size effect, the so-called *core-shell model* is proposed to show that the surface shell with a cubic structure covers the particle core with a tetragonal structure. In ferroelectric nanoparticles the core-shell model is in close relation with the particles size distribution. The spherical nanoparticle consists of two main parts: the core which is tetragonal (or ferroelectric) and the shell which is cubic (or paraelectric). The shell consists of an extremely distorted surface layer which partly is amorphous, partly a so-termed 'dead layer' and partly an extreme non-symetric crystal structure whereas the core consist of particles which are still tetragonal particles. The formation of core-shell structure has been demonstrated previously very successfully for ZnO nanoparticles (39; 40) where 8 nm core was embedded inside a 1 nm thick shell. Here, with the aid of analytical spectroscopic techniques our results also support the concept of core-shell model of ferroelectric nanoparticles where the nanoparticle consists of ferroelectric tetragonal-core and an outer tetragonal-to-cubic gradient-shell. When going to ultrafine particle size, outer gradient-shell effects increasingly dominates the tetragonal-core contributions, thus readily explaining the size driven tetragonal-to-cubic phase transition. The same effect has been already observed by NMR and EPR for Mn^{2+}:$BaTiO_3$ (8) and Cr^{3+}:$PbTiO_3$ (16).
The mean particle sizes were determined from X-ray diffraction, based on the single-line method. The details of the method were given in our previous study on nano-sized $PbTiO_3$ powders. The size distributions after milling are not Gaussian or Lorentzian, they rather resemble to log-normal functions.

4. Defect chemistry of ferroelectric nano-powders

To formally describe defects, such as lattice vacancies for instance, and dopant ions in the solid state, the *Kröger-Vink* notation is commonly used (41). In the framework of this notation, ions with lower valence than the one they replace (*acceptors*) are designated by a bar (A'_B) and ions with higher valence (*donors*) by a dot ($D^{\bullet}_B$). With that respect, the number of bars or dots

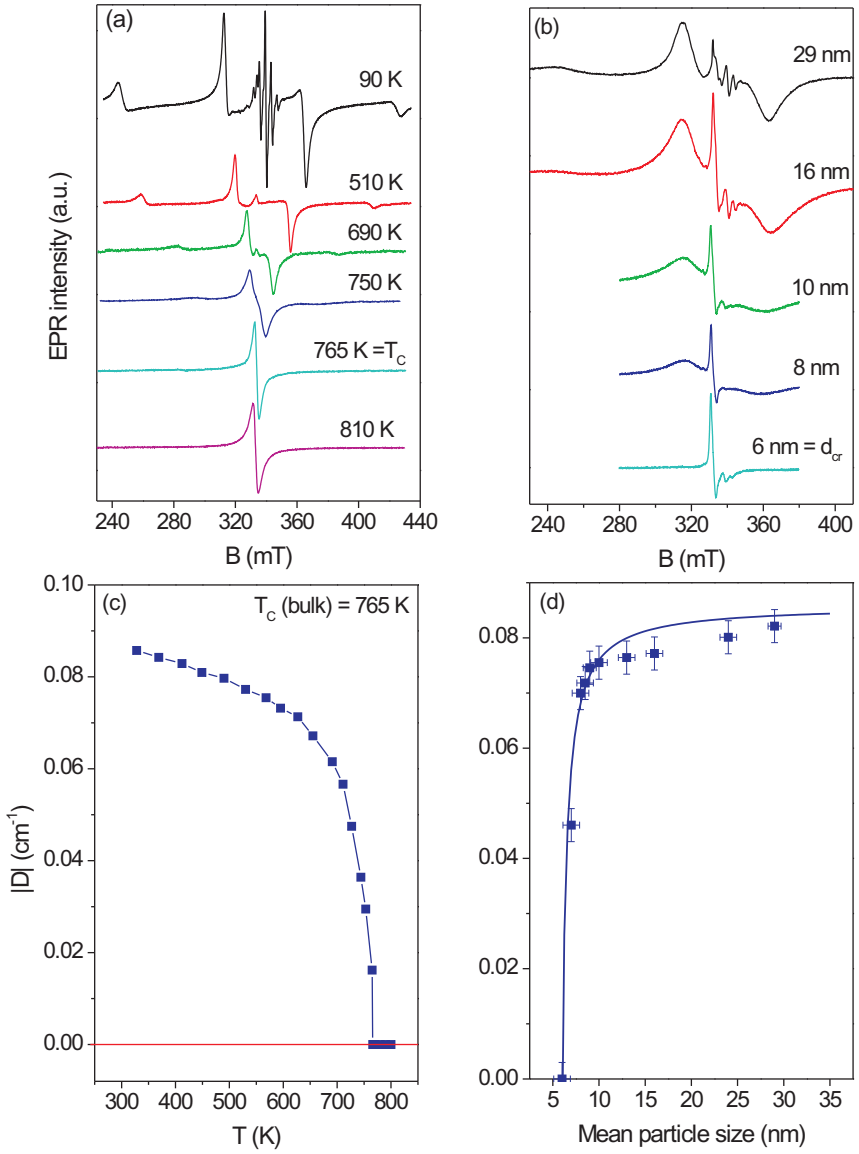

Fig. 5. (a,b) - X-band EPR spectra of Cr^{3+}-doped $PbTiO_3$. (a) - temperature dependent EPR spectra of bulk Cr^{3+}:$PbTiO_3$. (b) - size-dependent EPR spectra of Cr^{3+}:$PbTiO_3$ nano-powders measured at ambient temperature. (c,d) - phase transition monitored via the axial fine-structure parameter D.

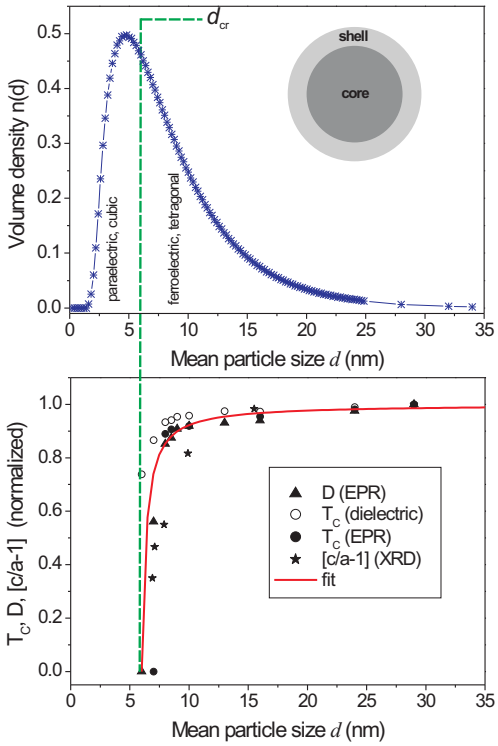

Fig. 6. The log-normal distributuion of particle sizes (top) and the drastic reduction of physical parameters by reducing the size below 10 nm (below).

designates the relative charge mismatch. The subscript defines the lattice site at which the considered defect is incorporated. In case the valence of both ions is equal, the superscript is a cross ($B_B^{\times}$). Interstitials are defined by an i as subscript, lattice vacancies - such as oxygen vacancies for instance – are given by $V_O^{\bullet\bullet}$ and electronic charge carriers by e'. The validity of the Kröger-Vink notation is, however, restricted to *dilute* defects that do not interact with each other.

For the here considered oxide perovskite ferroelectrics, the most relevant defects are *cation vacancies* (lead vacancies, V''_{Pb}), *anion vacancies* (oxygen vacancies, $V_O^{\bullet\bullet}$), *acceptor*-type ions with a lower positive charge than the ion they replace (e.g. Fe^{3+} for Ti^{4+}, Fe'_{Ti}), or *donor*-type ions with a higher positive charge than the ion they replace (e.g. Gd^{3+} for Pb^{2+}, $Gd^{\bullet}_{Pb}$).

With respect to the reaction of incorporation for Fe_2O_3 and Gd_2O_3 into $PbTiO_3$, the standard oxide reaction scheme for the synthesis of lead titanate is considered

$$PbO + TiO_2 \longrightarrow Pb_{Pb}^{\times} + Ti_{Ti}^{\times} + 3O_O^{\times} \tag{2}$$

With respect to the doping with Fe_2O_3, the oxide of the acceptor contains less oxygen per cation (Fe_2O_3) than the binary oxide of the host cation it replaces (TiO_2). Accordingly, the substitution of an acceptor oxide for the host oxide results in the introduction of an equivalent number of oxygen vacancies according to the *incorporation reaction*

$$Fe_2O_3 \xrightarrow{2TiO_2} 2Fe'_{Ti} + 3O^{\times}_{O} + V^{\bullet\bullet}_{O} \tag{3}$$

Additional to the oxygen vacancies generated by means of acceptor doping, a second source for the existence of oxygen vacancies peculiar to lead-containing materials consists in the loss of the volatile PbO component during high-temperature treatment (42) owing to the *defect equilibrium*

$$Pb^{\times}_{Pb} + O^{\times}_{O} \rightleftharpoons PbO(g) + V''_{Pb} + V^{\bullet\bullet}_{O} \tag{4}$$

creating *Schottky*-defect pairs.

An important issue for ferroelectric compounds are the diffusion properties of the above introduced defects. In that respect, the $V^{\bullet\bullet}_{O}$ will be rather mobile down to ambient temperature, because there are always nearest-neighbor oxygen sites in the perovskite structure with which the $V^{\bullet\bullet}_{O}$ may exchange their position. On the other hand, the V''_{Pb} and Fe'_{Ti} have no nearest-neighbor cation sites, for which reason they are rather immobile and their diffusion may only be observed at considerably higher temperatures (generally above about 1000 °C). Consequently, only the $V^{\bullet\bullet}_{O}$ contribute to the ionic conductivity of perovskite compounds at moderate temperatures.

In the so-termed *extrinsic regime*, where the concentration of defects is above a limit in which the defects may be regarded as *isolated*, the interaction of oppositely charged defects, such as negatively-charged acceptor dopants and positively charged oxygen vacancies, becomes important. Correspondingly, the ionic conductivity of the involved defects can be significantly reduced owing to the formation of defect complexes

$$Fe'_{Ti} + V^{\bullet\bullet}_{O} \rightleftharpoons (Fe'_{Ti} - V^{\bullet\bullet}_{O})^{\bullet} \tag{5}$$

where application of the law of mass action results in the following mass-action constant (43)

$$K_{Fe} = \frac{[(Fe'_{Ti} - V^{\bullet\bullet}_{O})^{\bullet}]}{[Fe'_{Ti}][V^{\bullet\bullet}_{O}]} \tag{6}$$

Generally, the magnitude of K is strongly dependent on the host system. Whereas for Fe^{3+}-doped $SrTiO_3$ at most half of the Fe^{3+} but all of the $V^{\bullet\bullet}_{O}$ are bound in defect complexes (43–45), for Fe^{3+}:$PbTiO_3$ exclusively $(Fe'_{Ti} - V^{\bullet\bullet}_{O})^{\bullet}$ defect complexes are formed and no 'free' Fe'_{Ti} could be observed for temperatures below 300 K (46). With this regard, Fe^{3+}:$BaTiO_3$ represents an intermediate situation (47–50), such that $K_{Fe:SrTiO_3} \leq K_{Fe:BaTiO_3} \leq K_{Fe:PbTiO_3}$ is valid.

Vice-versa, a donor-type dopant may reduce the concentration of oxygen vacancies in the lattice. This is owing to the reason that the oxide of a donor (Gd_2O_3) contains more oxygen per cation than the binary host oxide it replaces (PbO). Correspondingly, the excess oxygen serves to reduce the concentration of oxygen vacancies according to the following incorporation reaction

$$Gd_2O_3 + V^{\bullet\bullet}_{O} \xrightarrow{2PbO} 2Gd^{\bullet}_{Pb} + 3O^{\times}_{O} \tag{7}$$

For high donor-dopant concentration the oxygen vacancy concentration may thus be reduced to a very small amount characteristic of intrinsic ionic disorder. Alternatively, the donor

doping enhances the concentration of cation vacancies according to

$$Gd_2O_3 \xrightarrow{2PbTiO_3} 2Gd^{\bullet}_{Pb} + 3O^{\times}_{O} + V''_{Pb} \tag{8}$$

Contrary to the situation for acceptor-doping, for donor-doped $PbTiO_3$ compounds there is no formation of defect complexes between the donor ion and cation vacancies, such that the corresponding lattice defects ($Gd^{\bullet}_{Pb}$, V''_{Pb}) rather exist as 'isolated' centers (51).
A question that is still controversially discussed is the defect chemistry of co-doped compounds. These materials are simultaneously doped by an acceptor and a donor dopant, such as (Gd^{3+},Fe^{3+}):$PbTiO_3$ for instance. Two competing mechanisms for charge compensation are then conceivable; either the lattice vacancies generated by the two dopants cancel each other, or the defects formed add together. In the former scenario the amount of $V^{\bullet\bullet}_{O}$ would be considerably reduced by the donor doping and as consequence also the concentration of $(Fe'_{Ti} - V^{\bullet\bullet}_{O})^{\bullet}$ defect complexes should be decreased. Alternatively, the latter mechanism describes a situation where even in 'soft' co-doped compounds $(Fe'_{Ti} - V^{\bullet\bullet}_{O})^{\bullet}$ are present.

4.1 Defect-structure of acceptor-doped $PbTiO_3$ studied by EPR

The *'method-of-choice'* for the characterization of defect structure is provided by EPR spectroscopy (5; 52). The information content obtained from the analysis of the EPR spectra is twofold. First, it can be distinguished between 'isolated' Fe'_{Ti} functional centers and centers that have formed a $(Fe'_{Ti} - V^{\bullet\bullet}_{O})^{\bullet}$ defect complex for reasons of charge compensation. Second, the site symmetry at the Fe^{3+}-site is obtained, for which reason in case of a $(Fe'_{Ti} - V^{\bullet\bullet}_{O})^{\bullet}$ defect dipole, its orientation with respect to the orientation of the spontaneous polarization, P_S, in the $PbTiO_3$ nano-powders may be deduced (53). Correspondingly, the defect dipoles may be oriented either parallel $(Fe'_{Ti} - V^{\bullet\bullet}_{O})^{\bullet}_{\parallel}$ or perpendicular $(Fe'_{Ti} - V^{\bullet\bullet}_{O})^{\bullet}_{\perp}$ with respect to the orientation of P_S. In case of an 'isolated' Fe'_{Ti} center, an isotropic EPR line accounts for a cubic and paraelectric $PbTiO_3$ phase.
The corresponding EPR spectra for the obtained Fe^{3+}-modified $PbTiO_3$ nano-powders with varying mean grain size are given in figure 7. For comparison, also the EPR spectrum of a 'bulk' sample with mean grain size of about 500 nm is depicted (top). The spectrum consists of a dominant low-field peak at $\approx$ 100 mT characteristic for the existence of $(Fe'_{Ti} - V^{\bullet\bullet}_{O})^{\bullet}_{\parallel}$ defect complexes (54). As function of decreasing mean grain size, additional peaks occur in the EPR spectra, which may be explained by the following scenario: For nano-sized samples an increasing contribution arises from the surface of the nano-grains. According to a *core-shell model* (55; 56), this surface has cubic $PbTiO_3$ structure and thus is paraelectric. In cubic crystal symmetry, the advantage in energy of formation of an $(Fe'_{Ti} - V^{\bullet\bullet}_{O})^{\bullet}$ defect associate over the 'isolated' defects (Fe'_{Ti}, $V^{\bullet\bullet}_{O}$) (46) vanishes. Consequently, the observation of an isotropic EPR at $g = 2.002$ (figure 7(a), bottom) accounts for the existence of an isolated Fe'_{Ti} center in a paraelectric surface region. The third resonance at $\approx$ 150 mT is characteristic for a $(Fe'_{Ti} - V^{\bullet\bullet}_{O})^{\bullet}$ defect complex of rhombic site symmetry at the site of the Fe^{3+} functional center. Its origin may be twofold: First, it may be a $(Fe'_{Ti} - V^{\bullet\bullet}_{O})^{\bullet}_{\perp}$ defect dipole, oriented perpendicular to the direction of spontaneous polarization. Second, it may be a $(Fe'_{Ti} - V^{\bullet\bullet}_{O})^{\bullet}$ defect complex in a distorted crystal symmetry. Both scenarios agree with the existence of a distorted interface layer in the nano-crystals between the ferroelectric core and the paraelectric surface.
Schematically, the corresponding 'core-shell structure' is illustrated in figure 8. At the ferroelectric core of the $PbTiO_3$ nano-particles, $(Fe'_{Ti} - V^{\bullet\bullet}_{O})^{\bullet}_{\parallel}$ defect dipoles are formed that

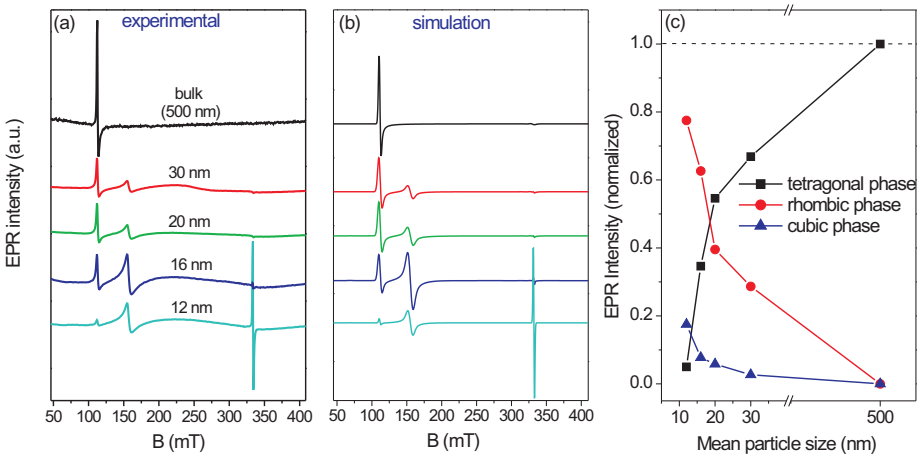

Fig. 7. (a,b) - X-band (9.4 GHz) EPR spectra of Fe^{3+}-doped $PbTiO_3$ nano-powders as function of mean grain size (indicated above the spectra). (a) - experimental spectra. (b) - numerical spectrum simulation. (c) - quantitative analysis of site symmetry as function of mean grain size, indicating the change in defect structure when approaching the nano-regime.

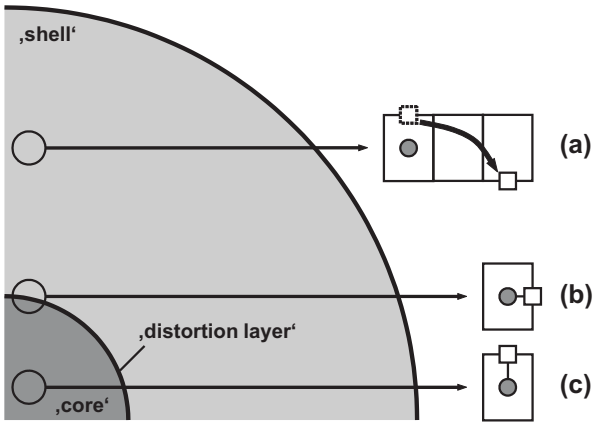

Fig. 8. Schematical illustration of the *'core-shell structure'* for Fe^{3+}-doped $PbTiO_3$ ferroelectric nano-particles. (a) - 'isolated' Fe'_{Ti} and $V_O^{\bullet\bullet}$ defects at the paraelectric surface. (b) - $(Fe'_{Ti} - V_O^{\bullet\bullet})^{\bullet}$ defect complexes of rhombic site symmetry at interface layer. (c) - $(Fe'_{Ti} - V_O^{\bullet\bullet})^{\bullet}_{\parallel}$ defect dipoles at the ferroelectric core. The corresponding unit cells are illustrated by rectangles, the Fe^{3+}-functional centers by a gray circle and the oxygen vacancies by open squares.

are aligned along the direction of spontaneous polarization. In contrast, at the paraelectric surface 'isolated' Fe'_{Ti} and $V_O^{\bullet\bullet}$ defects exist. This particularly impacts the ionic conductivity at the surface of $PbTiO_3$ nano-grains because the $V_O^{\bullet\bullet}$ act as ionic charge carriers when not

bound to $(Fe'_{Ti} - V_O^{\bullet\bullet})^{\bullet}$ defect complexes. In between ferroelectric core and the paraelectric surface region a distorted interface layer exists, which explains the existence of $(Fe'_{Ti} - V_O^{\bullet\bullet})^{\bullet}$ defect complexes of rhombic site symmetry.
Quantitatively, the amount of the three above mentioned defects is analyzed as function of the determined site symmetry as depicted in figure 7(c). Obviously, a marked *size-driven* change in defect structure is observed when comparing 'bulk' and nano-scale ferroelectrics.

4.2 Defect-structure of donor-doped $PbTiO_3$ studied by EPR

In contrast to the Fe^{3+} functional center in $PbTiO_3$ that is incorporated at the Ti-site and acts as an acceptor, the Gd^{3+}-center substitutes for Pb^{2+} at the A-site and hence acts as a donor. Furthermore, charge compensation is performed through the formation of lead vacancies in distant coordination spheres, such that no defect complexes are formed (51).
The corresponding X-band (9.4 GHz) and Q-band (34.1 GHz) EPR spectra of Gd^{3+}-doped $PbTiO_3$ nano-powders as compared to a 'bulk' compound are shown in figure 9. The nano-powders were obtained by HEBM for 10 h and subsequent calcination at various temperatures, yielding mean grain sizes in an interval between 50 and 500 nm.
The main result of the EPR-analysis is that the Gd^{3+} fine-structure interaction is only slightly reduced for decreasing mean grain size of the Gd^{3+}:$PbTiO_3$ nano-powders. Considerably more pronounced is an increased line-broadening owing to fine-structure strain. Adopting the above mentioned core-shell model also for the Gd^{3+}-doped $PbTiO_3$ nano-grains, the enhanced fine-structure strain can be rationalized by a superposition of EPR-resonances from Gd^{3+} functional center at the tetragonal core, the cubic shell and at the rhombic interface layer.
Considering the obtained EPR linewidths ΔB_{pp} for the two systems of nano-powders studied, a marked variation between the CPP-prepared Fe^{3+}-doped $PbTiO_3$ and the HEBM-obtained Gd^{3+}-doped $PbTiO_3$ nano-powders is observed. Whereas for the CPP-synthesis route almost no variation in ΔB_{pp} between the 'bulk' and the nano-scale materials can be determined, the HEBM-prepared nano-powders show a pronounced increase in ΔB_{pp}. This observation may be mainly traced back to the different distributions of grain size. Whereas the CPP-route provides nano-powders with log-normal distribution in grain size (15; 56), HEBM involves locally high temperature during the milling that increases the particle size and because comparatively long milling periods typically are required, the corresponding distribution in grain size is considerably larger (17; 18).

4.3 Defect chemistry of acceptor- and donor-doped nano-scale ferroelectrics

For 'bulk' $PbTiO_3$ compounds it is well established that the Fe^{3+} functional center acts as an acceptor and forms $(Fe'_{Ti} - V_O^{\bullet\bullet})^{\bullet}$ defect complexes for partial charge compensation (46; 57). According to the EPR results, each Fe^{3+} functional center is over-compensated by one oxygen vacancy. In order to obtain overall charge neutrality, exact charge compensation of two $(Fe'_{Ti} - V_O^{\bullet\bullet})^{\bullet}$ defect complexes is accomplished by one additional lead vacancy. Accordingly, the following defect equilibrium describes the 'bulk' situation in Fe^{3+}-doped $PbTiO_3$

$$2[V''_{Pb}] \approx [(Fe'_{Ti} - V_O^{\bullet\bullet})^{\bullet}] \tag{9}$$

The striking observation is that even though the Fe^{3+}-doping renders '*hard*' piezoelectric compounds, the $(Fe'_{Ti} - V_O^{\bullet\bullet})^{\bullet}$ defect dipole is positively charged for which reason it acts as a donor center in the equation for charge compensation.
The defect equilibrium, however, is drastically changed for Fe^{3+}-doped $PbTiO_3$ nano-powders where the Fe^{3+} functional centers rather exist as 'isolated' Fe'_{Ti}-centers that

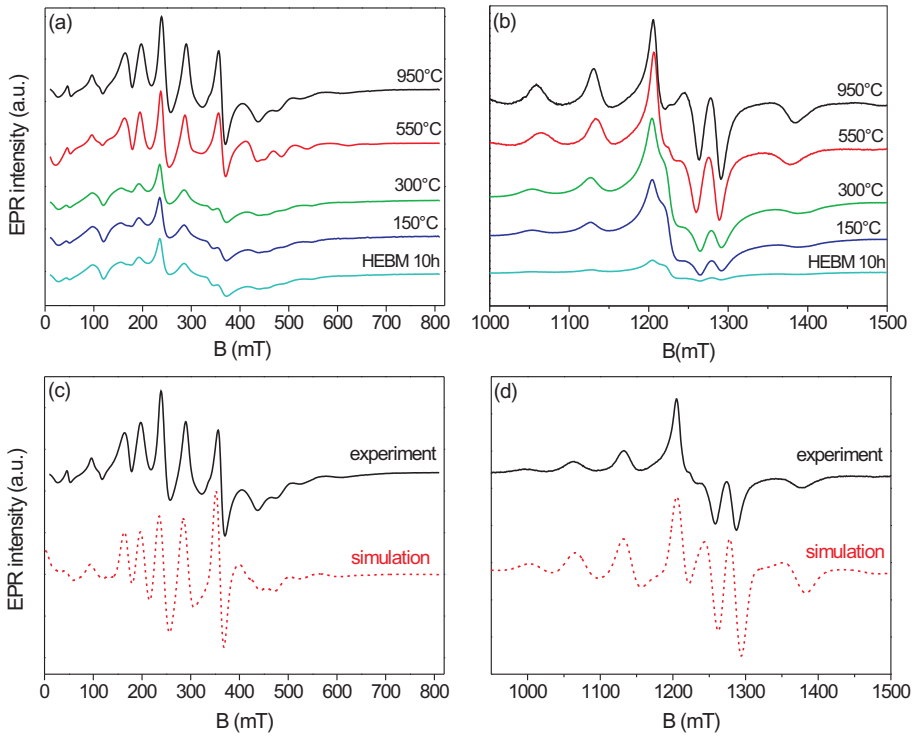

Fig. 9. (a,b) EPR spectra of Gd^{3+}-doped $PbTiO_3$ nano-powders as function of mean grain size after high-energy ball-milling for 10 h and subsequent calcination at various temperatures. (a,c) - X-band (9.4 GHz) EPR spectra. (b,d) - Q-band (34.1 GHz) EPR spectra. (c,d) - numerical spectrum simulations.

do not form $(Fe'_{Ti} - V_O^{\bullet\bullet})^{\bullet}$ defect complexes. For this reason, the defect equilibrium defined for the 'bulk' Fe^{3+}:$PbTiO_3$ compounds in equation (9), is modified to

$$[Fe'_{Ti}] \approx 2[V_O^{\bullet\bullet}] \tag{10}$$

Now the Fe'_{Ti} acts as an acceptor and the concentration of *mobile* oxygen vacancies is considerably enhanced because in the nano-regime the concentration of $(Fe'_{Ti} - V_O^{\bullet\bullet})^{\bullet}$ defect complexes is considerably decreased or even vanishes in the paraelectric state. This provides a means to explain the increased (ionic) conductivity often reported for nano-sized ferroelectric compounds (58). On the other hand, owing to the absence of $(Fe'_{Ti} - V_O^{\bullet\bullet})^{\bullet}$ defect dipoles, the '*hardening*' effect is expected to decrease for nano-sized materials. Furthermore, the defect equilibrium described in equation (10) necessitates no formation of V''_{Pb} for overall charge neutrality, as is required for 'bulk' compounds described in equation (9).
Contrary to the situation for 'hard' Fe^{3+}-doped $PbTiO_3$, for the 'soft' Gd^{3+}-doped $PbTiO_3$ compound there is no association of defect complexes that impacts the charge neutrality

condition. The donor-type $Gd^{\bullet}_{Pb}$-center necessitates a reduced concentration of oxygen vacancies but increased concentration of lead vacancies results according to

$$2[V''_{Pb}] \approx 2[V^{\bullet\bullet}_{O}] + [Gd^{\bullet}_{Pb}] \tag{11}$$

Here, no pronounced impact of the nano-regime on the defect structure is observed. Correspondingly, the defect-chemical mechanisms established for 'soft' ferroelectric compounds can be directly transferred to nano-scale ferroelectrics.

5. Conclusion

In summary, two main results emerge when studying nano-scale ferroelectrics. First, a *size-driven phase transition* occurs below a critical grain size and second, this ferro-to-paraelectric phase transition is accompanied by a pronounced *size-driven change in defect chemistry*.

Concerning the *size-driven phase transition*, the structural properties of spherical nano-particles can be explained by a *core-shell model*. According to this model, the nano-grains consist of a surface shell with a cubic structure that covers the particle core with a tetragonal structure. The nano-particles accordingly possess a ferroelectric core and an outer tetragonal-to-cubic gradient-shell. When going below an ultra-fine particle size, the outer gradient-shell effects increasingly dominates the tetragonal-core contributions, thus explaining the size driven tetragonal-to-cubic phase transition.

With respect to the *size-driven change in defect chemistry* of ferroelectric perovskite oxides, it has to be distinguished between acceptor- and donor-doped compounds. The defect complexes that exist in 'bulk' acceptor-doped materials vanish in the nano-regime, such that the 'hardening' effect is considerably decreased, whereas the ionic conductivity is increased. On the other hand, the defect-chemical mechanisms established for 'soft' ferroelectric compounds can be directly transferred to nano-scale ferroelectrics.

Finally, two effective methods have been introduced for the synthesis of ferroelectric nanoparticles. Both have advantages and drawbacks which can be summarized as follows: The Combined Pyrolysis and Polymerization (CPP) involves a precursor with subsequent calcinations that controls the particle size. This method easily allows incorporation of dopant ions in the form of metal acetylacetonates. With the need of this indirect technique, mean grain sizes down to about 10 nm can be reached. However, there is the possibility of agglomeration during calcinations, which may cause considerable size-distribution broadening. On the other hand, High Energy Ball Milling (HEBM) works without the need of wet chemistry (precursor) and subsequent high-temperature treatment (calcination). The particle size is controlled via the milling time through a mechanical alloying process. As starting material the corresponding metal oxides (also for doping) are used. This direct technique provides small particle sizes below 10 nm. However, high mechanical strain may cause large grain-size distributions.

6. Acknowledgements

We are very grateful for fruitful discussions and experimental support from many colleagues, particularly to Dr. Peter Jakes (Universität Freiburg), Prof. Mehmet Somer (Koc University Istanbul), Dr. S.K.S. Parashar (KIIT University India), Prof. Donald M. Smyth (Lehigh), Prof. Rolf Böttcher (University of Leipzig), Dr. H.-J. Gläsel, Dr. Hartmann (IOM Leipzig) Dr. A. Bartasyte (CNRS-INP Grenoble-Minatec), Prof. H. Rumpf (Universität Bonn), and Prof. J.

Banys (University of Vilnius). Financially, this research has been supported by the DFG center of excellence 595.

7. References

[1] Scott, J. F. (2000). *Ferroelectric Memories*, Springer, Berlin.
[2] Waser, R. (2005). *Nanoelectronics and Information Technology*, Wiley.
[3] Setter, N. (2002). *Piezoelectric Materials in Devices*, Swiss Federal Institute of Technology, Lausanne.
[4] Smyth, D. M. (2000). *The Defect Chemistry of Metal Oxides*, Oxford University Press, New York.
[5] Eichel, R.-A. (2008). *J. Am. Ceram. Soc.*, Vol. 91, 691.
[6] Morozov, M.I.; Damjanovic, D. (2010). *J. Appl. Phys.*, Vol. 107, 034106.
[7] Rüdiger, A.; Schneller, T.; Roelofs, A.; Tiedke, S.; Schmitz, T.; Waser, R. (2005). *Appl. Phys. A*, Vol. 80, 1247.
[8] Böttcher, R.; Klimm, C.; Michel, D.; Semmelhack, H. C.; Völkel, G.; Gläsel, H. J.; Hartmann, E. (2000). *Phys. Rev. B*, Vol. 62, 2085.
[9] Eichel, R.-A.; Erünal, E,; Drahus, M.D.; Smyth, D.M.; van Tol, J.; Acker, J.; Kungl, H.; Hoffmann, M.J. (2009). *Phys. Chem. Chem. Phys.*, Vol. 11, 8698.
[10] Erünal, E.; Eichel, R.-A.; Körbel, S.; Elsässer, C.; Acker, J.; Kungl, H.; Hoffmann, M.J. (2010). *Funct. Mat. Lett.* Vol. 3, 19.
[11] Hu, Y. M.; Gu, H. S.; Chen, W. P.; Wang Y. (2010). *Mater. Chem. Phys.*, Vol. 121, 10.
[12] Fukui, T. (1998). *J. Sol-Gel Sci. Tech.*, Vol. 11, 31.
[13] Zorel, H. E.; Ribeiro, C. A.; Crespi, M. S. (2001). *J. Mater. Sci. Lett.*, Vol. 20, 621.
[14] Selbach, S. M.; Wang, G.; Einarsrud,M.-A.; Grande, T. (2007). *J. Amer. Cer. Soc.*, Vol. 90, 2649.
[15] Erdem, E; Böttcher, R.; Semmelhack, H.-C.; Gläsel, H.-J.; Hartmann, E.; Hirsch, D. (2003). *J. Mater. Sci.*, Vol. 38, 3211.
[16] Erdem, E; Kiraz, K.; Somer, M.; Eichel, R.-A. (2010). *J. Eur. Ceram. Soc.*, Vol. 30, 289.
[17] Parashar, S. K. S.; Choudhary, R. N. P.; Murty, B. S. (2003). *J. Appl. Phys.*, Vol. 94, 6091.
[18] Parashar, S. K. S.; Choudhary, R. N. P.; Murty, B. S. (2004). *Mat. Sci. Eng. B*, Vol. 110, 58.
[19] Gläsel, H. J.; Hartmann, E.; Hirsch, D.; Böttcher, R.; Klimm, C.; Michel, D.; Semmelhack, H. C.; Hormes, J.; Rumpf, H. (1999). *J. Mater. Sci.*, Vol. 34, 2319.
[20] Lines, M. E.; Glas, A. M. (2001). *Principles and Applications of Ferroelectrics and Related Materials*, Oxford, Great Britain.
[21] Xu, Y. (1991). *Ferroelectric Materials and Their Applications*, North Holland, Amsterdam.
[22] Strukov, B. A.; Levanyuk, A. P. (1998). *Ferroelectric Phenomena in Crystals: Physical Foundations*, Springer, Berlin.
[23] Kretschmer, R.; Binder, K. (1979). *Phys. Rev. B*, Vol. 20, 1065.
[24] Tilley, D. R.; Zeks, B. (1984). *Sol. Stat. Commun.*, Vol. 49, 823.
[25] Glinchuk, M. D.; Eliseev, E. A.; Stephanovich, V. A. (2002). *Physica B-Condens. Matter*, Vol. 322, 356.
[26] Zhong, W. L.; Wang, Y. G.; Zhang, P. L.; Qu, B. D. (1994). *Phys. Rev. B*, Vol. 50, 698.
[27] Wang, C. L.; Smith, S. R. P. (1995). *J. Phys. Condens. Matter*, Vol. 7, 7163.
[28] Rychetsky, I; Hudak, O (1997). *J. Phys. Condens. Matter*, Vol. 9, 4955.
[29] Sheshadri, K.; Lahiri, R.; Ayyub, P.; Bhattacharya, S. (1999). *J. Phys. Condens. Matter*, Vol. 11, 2459.
[30] Glinchuk, M. D.; Morozovskaya, A. N. (2003). *phys. statu. solidi B*, Vol. 238, 81.
[31] Glinchuk, M. D.; Bykov, P. I. (2004). *J. Phys. Condens. Matter*, Vol. 16, 6779.

[32] Devonshire, A. F. (1949). *Philosophical Magazine*, Vol. 40, 1040.
[33] Ishikawa, K.; Yoshikawa, K.; Okada, N. (1988). *Phys. Rev. B*, Vol. 37, 5852.
[34] Shih, W. Y.; Shih, W. H.; Aksay, I. A. (1994). *Phys. Rev. B*, Vol. 50, 15575.
[35] Morozovska, A. N.; Glinchuk, M. D; Eliseev, E. A. (2007). *Phys. Rev. B*, Vol. 76, 014102.
[36] Burns, G.; Scott, B. A. (1973). *Phys. Rev. B*, Vol. 7, 3088.
[37] Mesquita, A.; Michalowicz, A.; Mastelaro, V. R. (2009). *Journal of Physics: Conference Series*, Vol. 190, 012081.
[38] Vedrinskii, R. V.; Kraizman, V. L.; Novakovich, A. A.; Demekhin, P. V.; Urazhdin, S. V. (1998). *J. Phys. Condens. Mat.* Vol. 10, 9561.
[39] Schneider, J. J.; Hoffmann, R. C.; Engstler, J.; Dilfer, S.; Klyszcz, A.; Erdem, E; Jakes, P.; Eichel, R.-A. (2009). *J. Mater. Chem.*, Vol. 19, 1449.
[40] Schneider, J. J.; Hoffmann, R. C.; Engstler, J.; Erdem, E; Jakes, P.; Eichel, R.-A.; Bauermann, L.-P.; Bill, J. (2010). *Chem. Mater.*, Vol. 22, 2203.
[41] Kröger, F.A.; Vink, H. J.(1956). In: *Solid State Physics*, Seitz, F.; Turnbull, D. (Ed.), Vol. 3, 273.
[42] Holman, R. L.; Fulrath, R. M. (1973). *J. Appl. Phys.*, Vol. 44, 5227.
[43] Merkle, R.; Maier, J. (2003). *Phys. Chem. Chem. Phys.*, Vol. 5, 2297.
[44] Kirkpatrick, E. S.; Müller, K. A.; Rubins, R. S. (1964). *Phys. Rev.*, Vol. 135, A86.
[45] Waldkirch, T. von; Müller, K. A.; Berlinger, W. (1972). *Phys. Rev. B*, Vol. 5, 4324.
[46] Meštrić, H.; Eichel, R.-A., Kloss, T.; Dinse, K.-P.; Laubach, So.; Laubach, St.; Schmidt, P.C. (2005). *Phys. Rev. B*, Vol. 71, 134109.
[47] Siegel, E.; Müller, K. A. (1979). *Phys. Rev. B*, Vol. 20, 3587.
[48] Possenriede, E.; Schirmer, O. F.; Donnerberg, H. J.; Godefroy, G.; Maillard, A. (1989). *Ferroelectrics*, Vol. 92, 245.
[49] Kornienko, S.M.; Bykov, I. P.; Glinchuk, M. D.; Laguta, V. V.; Belous, A. G.; Yastrabik, L. (1999). *Phys. Solid State*, Vol. 41, 1688.
[50] Böttcher, R.; Langhammer, H. T.; Müller, T.; Abicht, H. P. (2008). *J. Phys. Condens. Matter*, Vol. 20, 505209.
[51] Eichel, R.-A.; Meštrić, H.; Kungl, H.; Hoffmann, M. J. *Appl. Phys. Lett.*, Vol. 92, 122506.
[52] Eichel, R.-A. (2007). *J. Electroceramics*, Vol. 19, 9.
[53] Erdem, E.; Eichel, R.-A.; Kungl, H.; Hoffmann, M. J.; Ozarowski, A.; van Tol, H.; Brunel, L. C. (2007). *Phys. Script.*, Vol. T129, 12.
[54] Meštrić, H.; Eichel, R.-A.; Dinse, K.-P.; Ozarowski, A.; van Tol, J.; Brunel, L. C. (2004). *J. Appl. Phys.*, Vol. 96, 7440.
[55] Aoyagi, S.; Kuroiwa, Y.; Sawada, A.; Kawaji, H.; Atake, T. (1973). *J. Thermal Analy. Calor.*, Vol. 81, 627.
[56] Erdem, E; Semmelhack, H.-C.; Böttcher, R.; Rumpf, H.; Banys, J.; Matthes, A.; Gläsel, H.-J.; Hirsch, D.; Hartmann, E. (2006). *J. Phys. Condens. Matter*, Vol. 18, 3861.
[57] Erdem, E.; Drahus, M. D.; Eichel, R.-A.; Kungl, H.; Hoffmann, M. J.; Ozarowski, A.; van Tol, H.; Brunel, L. C. (2008). *Funct. Mat. Lett.*, Vol. 1, 7.
[58] Guo, X.; Pithan, C.; Ohly, C.; Jia, C. L.; Dornseiffer, J.; Haegel, F. H.; Waser R. (2005). *Appl. Phys. Lett.* Vol. 86, 082110.

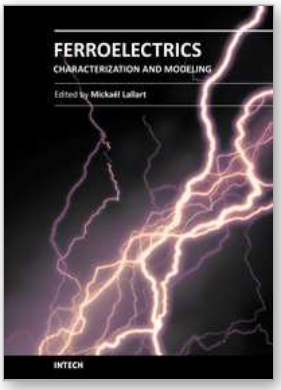

Ferroelectrics - Characterization and Modeling

Edited by Dr. MickaÃ«l Lallart

ISBN 978-953-307-455-9
Hard cover, 586 pages
Publisher InTech
Published online 23, August, 2011
Published in print edition August, 2011

Ferroelectric materials have been and still are widely used in many applications, that have moved from sonar towards breakthrough technologies such as memories or optical devices. This book is a part of a four volume collection (covering material aspects, physical effects, characterization and modeling, and applications) and focuses on the characterization of ferroelectric materials, including structural, electrical and multiphysic aspects, as well as innovative techniques for modeling and predicting the performance of these devices using phenomenological approaches and nonlinear methods. Hence, the aim of this book is to provide an up-to-date review of recent scientific findings and recent advances in the field of ferroelectric system characterization and modeling, allowing a deep understanding of ferroelectricity.

InTech Europe
University Campus STeP Ri
Slavka Krautzeka 83/A
51000 Rijeka, Croatia
Phone: +385 (51) 770 447
Fax: +385 (51) 686 166
www.intechopen.com

InTech China
Unit 405, Office Block, Hotel Equatorial Shanghai
No.65, Yan An Road (West), Shanghai, 200040, China
中国上海市延安西路65号上海国际贵都大饭店办公楼405单元
Phone: +86-21-62489820
Fax: +86-21-62489821